Supporting Information

High performance framework-integrated $Ni(OH)_2$ anodes for membraneless decoupled water splitting

*Tao Zhou [1, a], Kunlang Lu [1, a], Tao Li [a, *], Rui Xiao [a, *]*

[a] Key Laboratory of Energy Thermal Conversion and Control of Ministry of Education, School of Energy and Environment, Southeast University, Nanjing, 210096, China.

[1] These authors contributed equally to this work.

[*] Corresponding author. E-mail address: 101012902@seu.edu.cn and ruixiao@seu.edu.cn

Calculation of Faradaic efficiency

A well-sealed decoupled alkaline water-splitting cell was used to produce H_2 under a constant current of 50 mA cm^{-2} for 300 s. Meanwhile, the H_2 yield was quantitatively determined using a typical water-displacement method. Faradaic efficiency (η_F) is calculated according to the following formula:

$$\eta_F = \frac{n \times V \times F}{V_m \times I \times t} \quad (1)$$

where n is the number of electron transfer (n = 2), V is produced gas volume (L), F is Faraday constant (96485 C mol^{-1}), V_m is volumetric Avogadro number (24.5 L mol^{-1}), I is the applied current (A), and t is the reaction time (s).

The electrical energy consumption for hydrogen generation was calculated from the hydrogen-production voltage (U_{cell}) and Faradaic efficiency (η_F) using the following formula:

$$E_{H_2}(kWh / m^3_{H_2}) = \frac{\int_0^t U_{cell}(t) I_{cell}(t) dt}{V} \quad (2)$$

Thermal regeneration test

The framework-integrated $Ni(OH)_2$ anode was galvanostatically charged at 15 mA cm^{-2} for different durations (t_c = 5, 10, 20, 40, 60, and 90 min). The charged $Ni(OH)_2$ anode was then immersed in 5 M KOH at different regeneration temperatures (T_{regen} = 75, 85, and 95 °C) for corresponding regeneration times (t_{regen} = 5, 10, 20, 40, 60, and 90 min). After regeneration, the

anode was discharged under the same conditions to 0 V (vs. Hg/HgO), the discharge duration(t_{dis}) was recorded, and the regenerated charge density (Q_R, C cm^{-2}) was calculated according to:

$$Q_R = I_c \times (t_c - t_{dis}) \quad (3)$$

Where I_c is the charging current (15 mA cm^{-2}), t_c is charging duration (s) and t_{dis} is discharging duration (s).

Heat loss calculation

To evaluate the overall energy efficiency of decoupled water splitting, the main heat losses in the cell were quantified. The main heat-loss contributions considered in the model include heating of the $Ni(OH)_2$ anode and cathode, heat dissipation through the cell walls, and the endothermic oxidation of $Ni(OH)_2$ to NiOOH during the charging step. In addition to this heat loss, make-up water must be heated from 25 °C to 95 °C to compensate for the water consumed during the thermal regeneration step, where NiOOH is converted back to $Ni(OH)_2$. The heat losses associated with the cathode ($q_{cathode}$) and the cell walls (q_{wall}) were not measured directly in this work but were taken from the literature[1]. The heat loss incurred by the anode and the make-up water were calculated as:

$$q_{loss} = q_{loss,anode} + q_{loss,water} = m_{Ni(OH)_2,active} \int_{25°C}^{95°C} C_{pNi(OH)_2} dT + m_{H_2O} \int_{25°C}^{95°C} C_{pH_2O} dT \quad (4)$$

Where C_p designates heat capacity (J g^{-1} K^{-1}). The mass of active $Ni(OH)_2$ can be calculated according to:

$$m_{Ni(OH)_2,active} = \frac{Q_R \eta_F M_W}{zF} \quad (5)$$

Where Q_R is the regenerated charge, M_W = 92.7 g mol^{-1} is the molar mass of nickel hydroxide, and z =1 is the number of electrons transferred per $Ni(OH)_2$ molecule. In addition to heat loss, heat gain also occurs during the thermal regeneration stage due to the exothermic regeneration reaction, and it can be calculated according to the following formula:

$$q_{gain} = m_{Ni(OH)_2,active} \Delta H_{rxn} \quad (6)$$

where ΔH_{rxn} = -83 J $g_{Ni(OH)2,active}^{-1}$ is the standard enthalpy change for the reaction.[2] This heat is generated only during the reactivation portion of the thermal regeneration stage for oxidized nickel hydroxide.

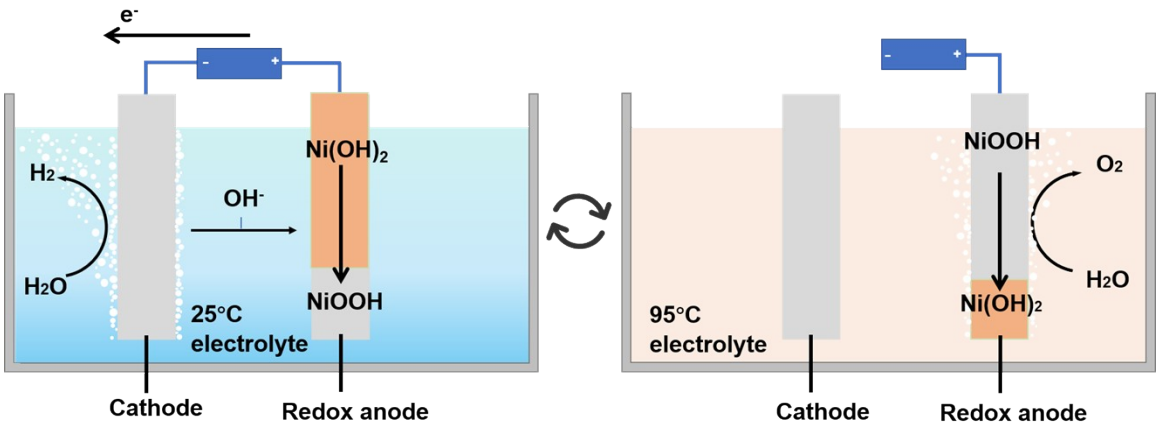

Fig. S1 Electrochemical–thermochemical cycle for decoupled water splitting.

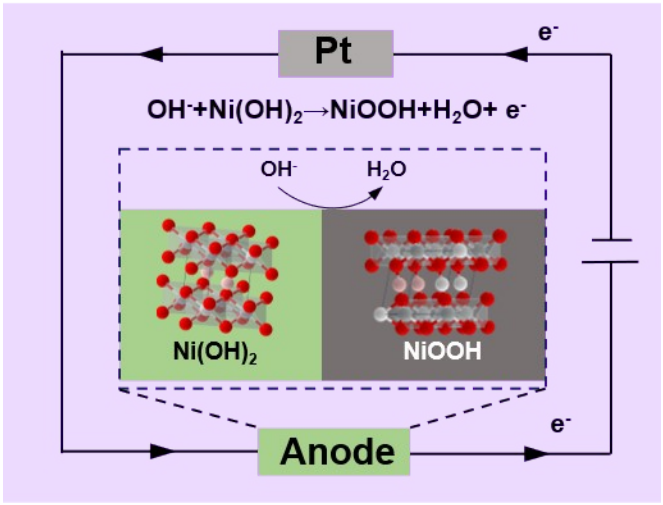

Fig. S2 Charge mechanism diagram of framework-integrated $Ni(OH)_2$ anode.

During the charging phase, driven by an external electric field, OH^- within the electrolyte migrate towards the electrode-electrolyte interface. Subsequently, they participate in an electrochemical reaction by extracting protons from the solid material phase, generating water and converting $Ni(OH)_2$ into NiOOH. The superhydrophilic interface significantly enhances the wettability between the electrode and the electrolyte, ensuring intimate interfacial contact. This accelerates OH^- transport and the interfacial deprotonation kinetics, thereby boosting

charging efficiency.[3, 4]

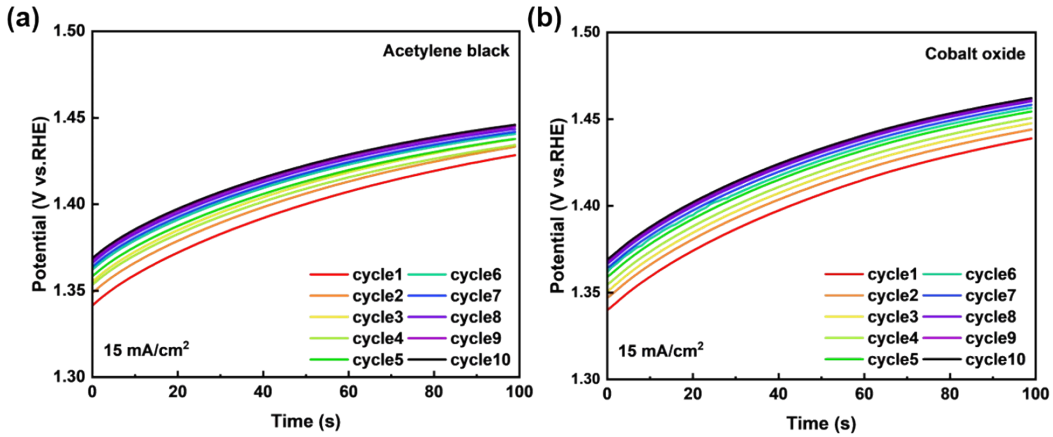

Fig. S3 Charging potential curves during ten decoupled water-splitting cycles.

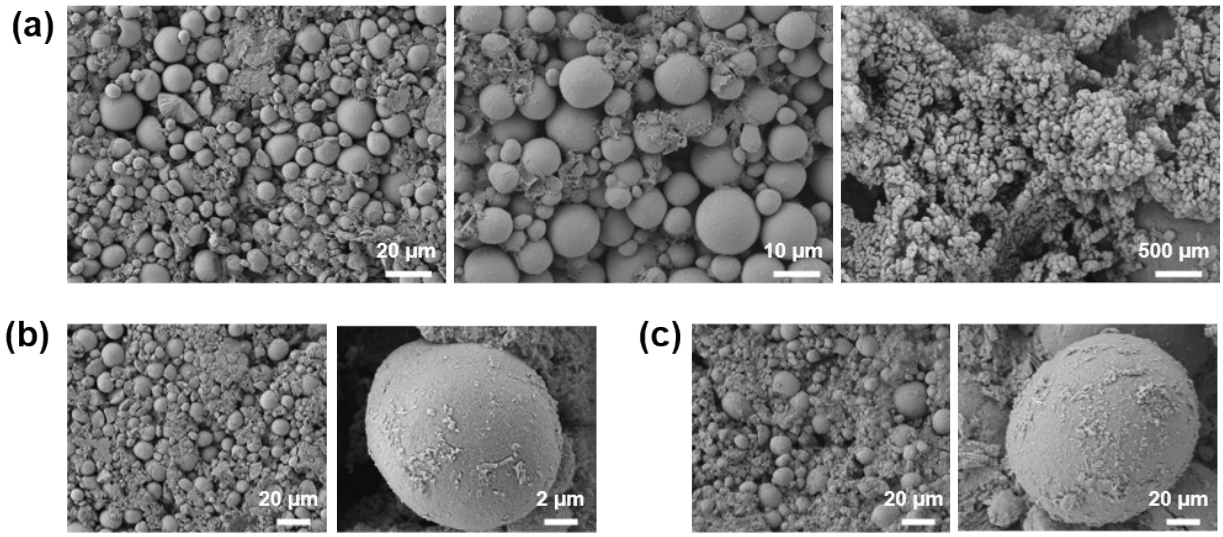

Fig. S4 SEM images of framework-integrated $Ni(OH)_2$ anodes prepared with different conductive additives as prepared. (a) nickel powder. (b) acetylene black. (c) cobalt oxide.

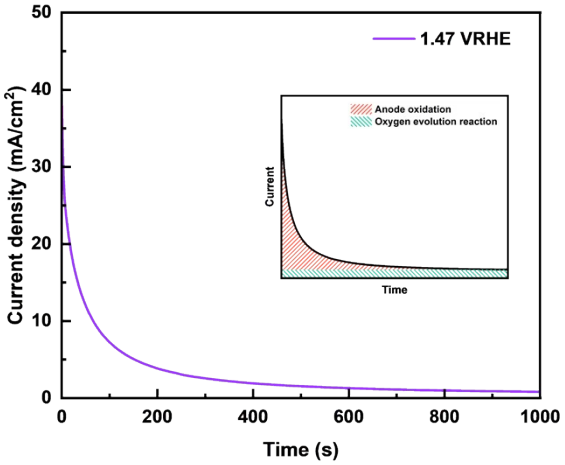

Fig. S5 Potentiostatic current traces for framework-integrated $Ni(OH)_2$ anodes.

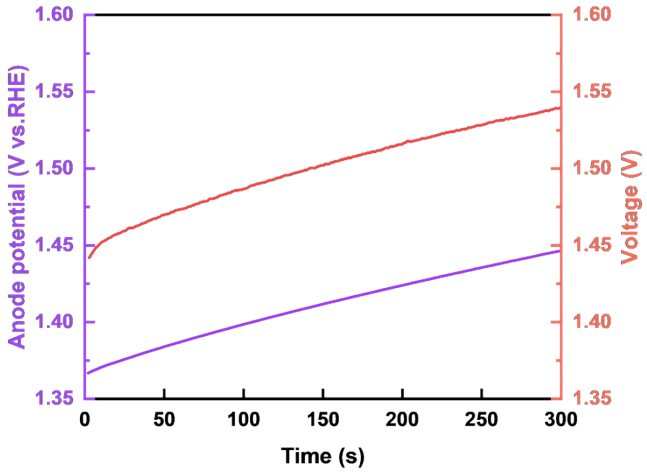

Fig. S6 Hydrogen-production voltage and the corresponding anodic potential during decouple water splitting at a current density of 50 mA cm^{-2}. The figure shows the average anodic potential (purple) and the corresponding hydrogen-production voltage (red) over 10 decouple water-splitting cycles.

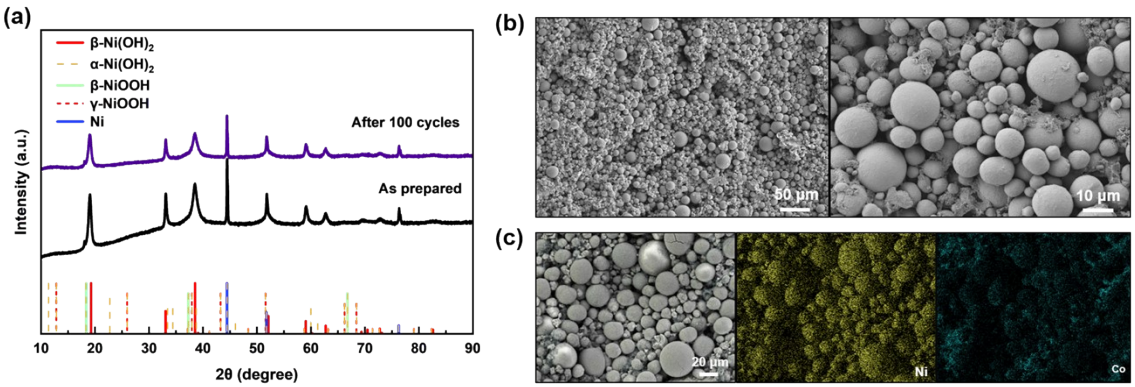

Fig. S7 (a) XRD patterns, (b) SEM images and (c) EDS images of the framework-integrated $Ni(OH)_2$ anode after 100 decoupled water-splitting cycles.

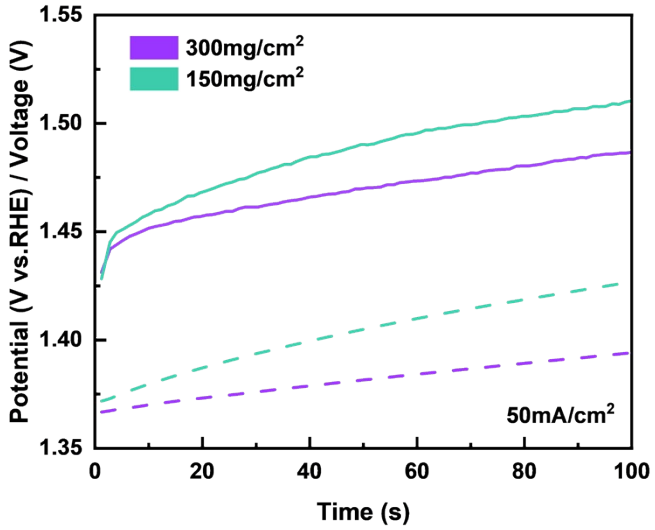

Fig. S8 Hydrogen-production voltage and corresponding anodic potential during decoupled water splitting using framework-integrated $Ni(OH)_2$ anodes with different loadings. Solid lines represent the hydrogen-production voltage, and dashed lines represent the corresponding anodic potential.

Increasing the $Ni(OH)_2$ areal loading from 150 to 300 mg cm^{-2} results in a lower hydrogen-production cell voltage and a lower average anode potential, indicating reduced polarization at higher loading. This behavior arises because, at a fixed geometric current density, a higher loading distributes the applied current over a larger amount of redox-active material, thereby

reducing the effective current per unit $Ni(OH)_2$. As a result, the kinetic overpotential required for the $Ni(OH)_2$/NiOOH conversion decreases, and the anode operates at a lower potential. This advantage becomes more important at elevated current densities, where higher loading helps mitigate polarization and improves decoupled water-splitting performance.

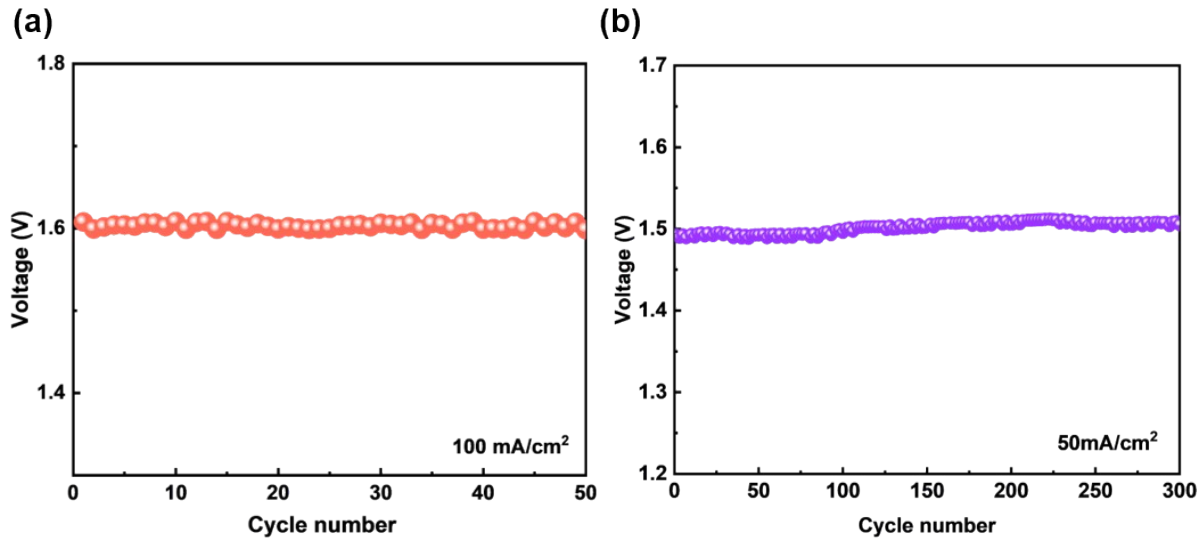

Fig. S9 (a) Cycling stability during decoupled water splitting with a 300 s hydrogen-production step at 100 mA cm^{-2}. (b) Electrochemical cycling stability of framework-integrated $Ni(OH)_2$ anode with a 300 s hydrogen-production step.

Further tests at a higher current density of 100 mA cm^{-2} (50 cycles) showed stable cyclability (Fig. S9a). However, the relatively high anodic potential triggers the competitive OER during the charging step. Thus, reducing the charging duration or operating current density is required to maintain strict decoupled operation. Additionally, extended electrochemical testing for 300 cycles at 50 mA cm^{-2} demonstrated a highly stable working potential of 1.50 V (Fig. S9b).

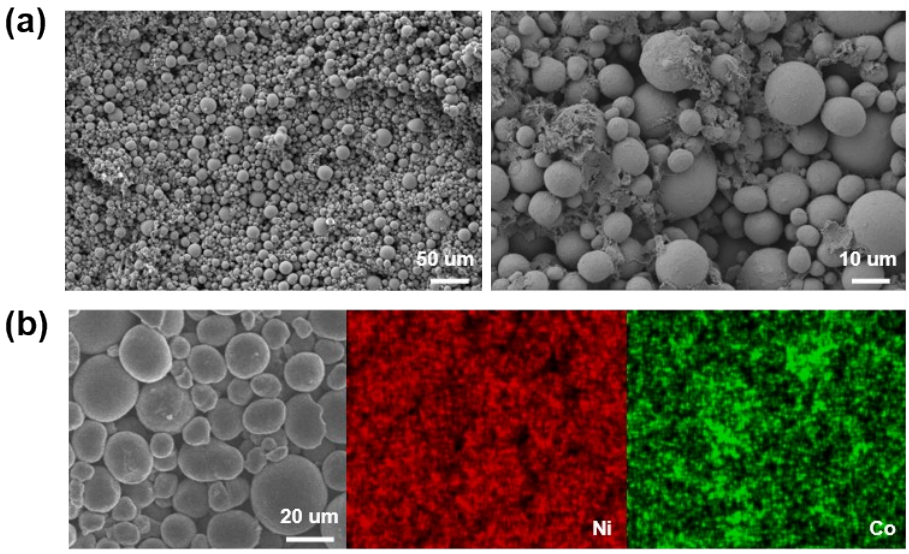

Fig. S10 (a) SEM images and (b) EDS images of the framework-integrated $Ni(OH)_2$ anode after 50 decoupled water-splitting cycles at 100 mA cm^{-2}.

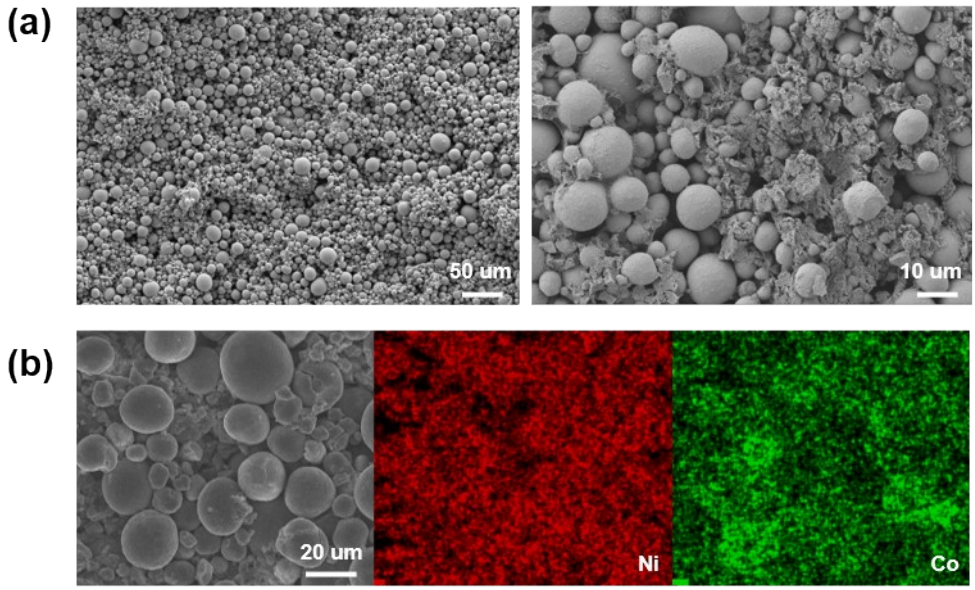

Fig. S11 (a) SEM images and (b) EDS images of the framework-integrated $Ni(OH)_2$ anode after 300 electrochemical cycles at 50 mA cm^{-2}.

Thermal Regeneration Performance

This work employs thermal regeneration to chemically reduce NiOOH to $Ni(OH)_2$, thereby completing the anode-regeneration step in the decoupled water-splitting cycle. To elucidate the

factors governing the thermal-regeneration capacity of the $Ni(OH)_2$ electrode, the framework-integrated $Ni(OH)_2$ anode was first galvanostatically charged to different input charge densities and then discharged under the same current density to 0 V (vs. Hg/HgO). As shown in Fig. S12a, when the input charge density was below 90 C cm^{-2}, the charge and discharge capacities were essentially identical, indicating negligible contributions from side reactions and a Coulombic efficiency close to 100% within this range. Therefore, the effective regenerated charge arising from thermal regeneration can be quantitatively determined based on charge conservation using Eq. (2). Furthermore, Fig. S12b shows the evolution of the regenerated charge density (Q_R) of the framework-integrated $Ni(OH)_2$ anode as a function of the total regeneration time at different regeneration temperatures. At a given regeneration time, Q_R increases markedly with temperature. For example, when the temperature is raised from 75 to 95 °C, the regenerated charge density increases from 5.56 to 7.34 C cm^{-2}. This accelerated regeneration at higher temperature is consistent with the thermodynamic and kinetic characteristics of the NiOOH-to-$Ni(OH)_2$ chemical regeneration reaction. Thermodynamically, the oxygen-evolution nature of the regeneration process is associated with a positive entropy change, and increasing temperature enhances the driving force. Kinetically, the reaction involves proton diffusion and structural rearrangement within the layered NiOOH lattice, which are thermally activated processes and are therefore significantly promoted at elevated temperatures. Notably, most of the regenerated charge is produced during the initial stage of thermal regeneration, after which the growth rate gradually decreases, suggesting that the reaction initiates at the electrode/electrolyte interface

and then propagates into the electrode interior in a diffusion-limited manner. Therefore, 95 °C was selected to enable efficient and reproducible regeneration within a practical time frame. In addition, Fig. S12c indicates a positive correlation between Q_R and the initial state of charge (SOC). The regenerated charge density increases significantly with increasing SOC. This can be attributed to the higher fraction of NiOOH and a larger reactive interfacial area at higher SOC, which enhances the effective driving force and accelerates the overall reduction kinetics.

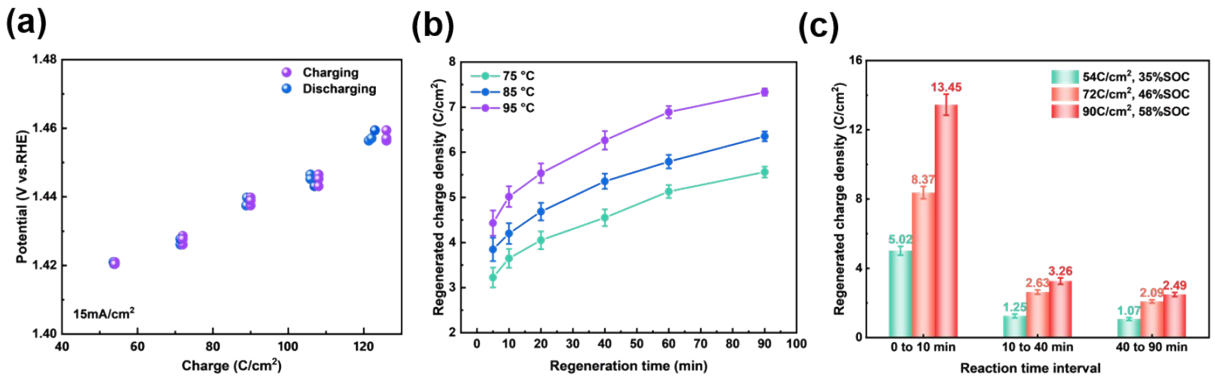

Fig. S12 (a) Relationship between the polarization potential of the framework-integrated $Ni(OH)_2$ anode and the charging capacity. (b) Regenerated charge density of the framework-integrated $Ni(OH)_2$ anode at different regeneration temperatures. (c) Regenerated charge density of the framework-integrated $Ni(OH)_2$ anode with different initial states of charge (SOC).

Heat Loss

To evaluate the overall energy efficiency of decoupled water splitting, it is necessary to consider not only the electrical energy input for hydrogen production but also the associated heat losses. In the decoupled water-splitting cycle, the electrochemical hydrogen-generation step is carried out near ambient temperature and does not require external heating. In contrast, during the thermal regeneration step both the anode and the cathode must be heated from 25 °C to about 95 °C to drive the oxygen-release reaction, which inevitably introduces thermal

losses. The main contributions to these heat losses are as follows. (1) heating of the active $Ni(OH)_2$ anode and the cathode from 25 to 95 °C during the thermal regeneration stage; (2) heating the make-up water from 25 to 95 °C and feeding it into the system to compensate for the water consumed by the conversion of NiOOH back to $Ni(OH)_2$ during the thermal regeneration stage; (3) heat dissipation through the cell walls.

The results of the heat loss calculations are shown in Table S1. Under the operating conditions of 50 mA cm^{-2} and an average hydrogen-production voltage of 1.51 V, the electrical energy required for hydrogen production was 3.40 kWh m^{-3} H_2. The thermal loss associated with heating the anode from 25 to 95 °C is estimated to be 0.1 kWh m^{-3} H_2, while the heat required to warm the water consumed during the thermal regeneration step amounts to 0.046 kWh m^{-3} H_2. Heat losses from wall heating (0.18 kWh m^{-3} H_2) and cathode heating (0.0016 kWh m^{-3} H_2) were taken from a previously reported decoupled water-splitting study.[1] The application of these values is considered appropriate because our system employs a comparable cell hardware configuration, operates over a similar thermal regeneration temperature window (25 to 95 °C), and utilizes the same platinized titanium mesh cathode. Since these specific thermal-loss terms are primarily governed by macroscopic heat capacities and temperature gradients rather than the specific anodic redox kinetics, they serve as a reasonable estimate for the current energy analysis. In total, the net thermal loss of the system is estimated to be 0.21 kWh m^{-3} H_2. This analysis indicates that wall heating and anode heating dominate the thermal penalty. Improving insulation of the cell or regeneration vessel and tubing can directly reduce heat dissipation. Using low-heat-

capacity substrates and lightweight electrode or current-collector designs can further lower the sensible heat required for heating. Because the regeneration heating loss is approximately fixed per cycle, extending the hydrogen-production duration reduces the heat loss normalized to hydrogen production. Heat integration, such as recovering sensible heat and using the heat released during oxygen generation to preheat make-up water, could further reduce the net thermal loss.

Table S1 Calculated heat losses of the decoupled water-splitting test at an anodic current density of 50 mA cm^{-2} with a charging time of 300 s.

	NF-supported anode	Unit
Q_R	15	C cm^{-2}
η_F	97.3%	
m_{H2}	0.152	mg
$m_{Ni(OH)2,\ active}$	14.4	mg
$C_{pNi(OH)2}$	0.8847	J g^{-1} K^{-1}
q_{anode}	0.1	kWh m^{-3} H_2
m_{H2O}	1.36	mg
C_{pH2O}	4.1872	J g^{-1} K^{-1}
q_{H2O}	0.046	kWh m^{-3} H_2
$q_{cathode}$	0.0016	kWh m^{-3} H_2
q_{wall}	0.18	kWh m^{-3} H_2
ΔH_{rxn}	-83	J g^{-1}
q_{gain}	-0.12	kWh m^{-3} H_2
q_{total}	0.21	kWh m^{-3} H_2

Table S2 EDS compositional analysis of the framework-integrated $Ni(OH)_2$ anode.

Sample	SEM micrograph	EDS spectrum	Average atomic composition of cobalt(at.%)
As prepared	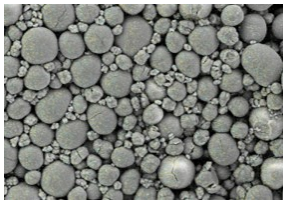	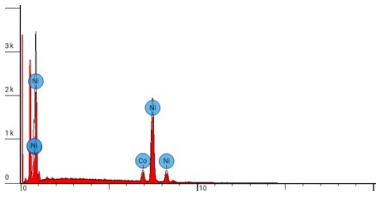	9.9%
After 100 decoupled water splitting cycles	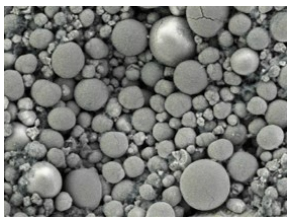	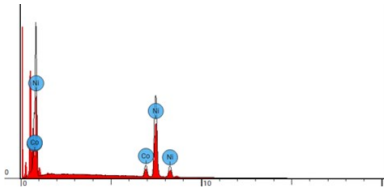	9.7%

Table S3 Comparison of different decoupled water electrolysis hydrogen production systems using solid redox mediators.

Solid redox mediators	Electrolyte	Current density (mA/cm^2)	Average cell voltage(V)[a] (and efficiency)[b]	Maximum running time	Efficiency	Ref.
$Ni(OH)_2$/NiOOH	5 M KOH	50	1.51 ($98\%_{HHV}$)	16.7h	97.3%	This work
Co–$Ni(OH)_2$/Co-NiOOH	5 M KOH	50	2.28 ($65\%_{HHV}$)	53 h	93.1%	[5]
NaNiHCF	NaOH/0.5 M H_2SO_4+1 M Na_2SO_4	20	1.77 ($84\%_{HHV}$)	8.3 h	98.6%	[6]
Co-$Ni(OH)_2$@NF	1 M KOH	8.3	1.83 ($81\%_{HHV}$)	20.2 h	100 %	[7]
$Ni(OH)_2$/NiOOH	1 M KOH	50	2.1 ($70\%_{HHV}$)	20 h	99.2%	[8]
$Ni(OH)_2$/NiOOH	1 M KOH	5	2.1 ($70\%_{HHV}$)	20h	100%	[9]
$Ni(OH)_2$/NiOOH	1 M KOH	20	2.0 ($74\%_{HHV}$)	33.3 h	94.7%	[10]
PTO	0.5 M H_2SO_4	5	1.66 ($89\%_{HHV}$)	70.8 h	98.7%	[11]

[a] The cell voltage is the sum of the hydrogen-evolution and oxygen-evolution voltages.

[b] The cell efficiency is calculated with respect to 1.48 V, corresponding to the higher heating value (HHV) of hydrogen.

Table S4 Faradaic efficiency of decoupled alkaline water electrolysis cell at 50 mA/cm^2.

Time (s)	Average H_2 volume (mL)	Faradaic efficiency (%)
0	0	0
100	2.46	96.8
200	4.94	97.4
300	7.44	97.8

Average Faradaic efficiency for H_2 production: 97.3%.

References

1. H. Dotan, A. Landman, S. W. Sheehan, K. D. Malviya, G. E. Shter, D. A. Grave, Z. Arzi, N. Yehudai, M. Halabi, N. Gal, N. Hadari, C. Cohen, A. Rothschild and G. S. Grader, *Nature Energy*, 2019, **4**, 786-795.
2. D. D. Macdonald and M. L. Challingsworth, *Journal of The Electrochemical Society*, 1993, **140**, 606.

3. H. He, J. Lian, C. Chen, Q. Xiong and M. Zhang, *Chemical Engineering Journal*, 2021, **421**, 129786.
4. R. Fu, C. Yu, S. Li, J. Yu, Z. Wang, W. Guo, Y. Xie, L. Yang, K. Liu, W. Ren and J. Qiu, *Green Chemistry*, 2021, **23**, 3400-3409.
5. T. Xiang, H. Ya, Z. Wang, X. Zhao, H. Xie, J.-B. He and C. Chen, *International Journal of Hydrogen Energy*, 2025, **170**, 151257.
6. F. Lv, Z. Qin, J. Wu, L. Pan, L. Liu, Y. Chen and Y. Zhao, *ChemSusChem*, 2023, **16**, e202201689.
7. Z. Nie, L. Zhang, Z. Du, J. Hu, X. Huang, C. Zhou, T. Wågberg and G. Hu, *Journal of Colloid and Interface Science*, 2023, **642**, 714-723.
8. M.-J. Zhao, Q. He, T. Xiang, H.-Q. Ya, H. Luo, S. Wan, J. Ding and J.-B. He, *Renewable Energy*, 2023, **203**, 583-591.
9. A. Landman, H. Dotan, G. E. Shter, M. Wullenkord, A. Houaijia, A. Maljusch, G. S. Grader and A. Rothschild, *Nature Materials*, 2017, **16**, 646-651.
10. L. Chen, X. Dong, Y. Wang and Y. Xia, *Nature communications*, 2016, **7**, 11741.
11. Y. Ma, Z. Guo, X. Dong, Y. Wang and Y. Xia, *Angewandte Chemie International Edition*, 2019, **58**, 4622-4626.